Optical determination of thermoelectric transport coefficients in a hot-carrier absorber

Thomas Vezin,[1,*] Hamidreza Esmaielpour,[2] Laurent Lombez,[3] Jean-François Guillemoles,[1] and Daniel Suchet[1]

[1] *UMR-IPVF 9006, CNRS, Ecole Polytechnique IPP, ENSCP PSL, Institut Photovoltaique d'Ile de France, Palaiseau, France*
[2] *Walter Schottky Institute and Physics Department, TUM School of Natural Sciences, Technical University of Munich, Garching, Germany*
[3] *INSA-CNRS-UPS, LPCNO, Universite de Toulouse, Toulouse, France*

(Received 20 February 2024; revised 27 June 2024; accepted 30 July 2024; published 9 September 2024)

Hot-carrier solar cells offer potential for enhancing the energy-conversion efficiency of photovoltaic devices. Transport properties of such systems remain largely unexplored but could hinder their efficiency. In this work, we develop a suitable framework for describing the thermoelectric ambipolar transport of photogenerated hot carriers and derive analytical expressions for the ambipolar transport coefficients that are valid even in the degenerate case. We demonstrate that these transport coefficients can be measured from hyperspectral photoluminescence imaging. We validate this experimental determination by showing its consistency with the Boltzmann transport equation in the relaxation-time approximation.

DOI: 10.1103/PhysRevApplied.22.034018

I. INTRODUCTION

"Hot carriers" denote carrier populations that deviate from thermal equilibrium with the surrounding lattice. Such populations arise following intense excitation, under the condition of strong intraband carrier interactions and weak coupling to the lattice [1–3]. Hot carriers are detrimental to microelectronic devices like transistors [4]. However, they have been thought to be beneficial for energy-conversion devices, particularly photocatalysis [5,6] and solar cells [7–11].

In the context of solar cells, hot carriers may lead to a voltage boost, ΔV, compared to a single-junction solar cell. Assuming isentropic extraction through perfectly selective contacts, [7]

$$e\Delta V = \frac{E_{\text{ext}} - \Delta\mu}{T_H}\Delta T, \tag{1}$$

where E_{ext} represents the energy at which electron-hole pairs are extracted by the selective contacts, $\Delta\mu$ is the quasi-Fermi-level splitting (QFLS) in the absorber, T_H is the carrier temperature, and $\Delta T = T_H - T_L$ is the difference between carrier and lattice temperatures.

This equation showcases the similarities between a hot-carrier solar cell and a thermoelectric generator. This parallel has provided an insightful framework to account for the extraction of hot carriers from the absorber towards a cold metal through energy-selective contacts [12–15]. An overlooked consequence is the influence of inhomogeneous temperature on coupled carrier and heat transport *within* the absorber [16–18].

To investigate such in-plane thermoelectric transport, photoluminescence (PL) imaging is a promising tool [19–21]. Broadband PL imaging has been utilized to measure isothermal ambipolar carrier diffusion in doped GaAs [22]. Then, the use of spectral resolution through hyperspectral imaging enabled the study of thermoelectric transport of hot carriers [16] and hot trions [18]. However, a comprehensive model of thermoelectric transport for hot carriers in the context of solar cells has not yet been established.

This is because this system explores unusual conditions for thermoelectricity. First, many thermoelectric investigations focus on determining material properties. In contrast, we study the thermoelectric properties of photogenerated populations that depend on excitation conditions, as in photo-Seebeck experiments [23]. Second, the intense optical excitation necessary for hot-carrier generation results in high carrier densities and strong electrostatic coupling between electrons and holes, leading to ambipolar diffusion [21]. Finally, we consider a situation with inhomogeneous optical excitation, which cannot be described with a constant QFLS, as typically assumed in most ambipolar derivations [24–26].

This article presents a framework for describing thermoelectric ambipolar transport of hot carriers, which is

---

[*] Contact author: thomas.vezin.x15@polytechnique.edu

valid even in the degenerate regime. We show that this framework resembles the usual thermoelectric transport equation, provided we use effective ambipolar transport coefficients. Experimentally, we use pointlike excitation to generate local hot-carrier distributions. We probe hot-carrier diffusion by mapping carrier densities and temperatures with micrometer resolution thanks to hyperspectral imaging. We show that the ambipolar Seebeck coefficient can be directly measured from this optical experiment. Finally, we perform numerical estimations based on the Boltzmann transport equation and show that they are consistent with our measurements.

II. AMBIPOLAR SEEBECK TRANSPORT

The situation considered in this work is pictured in Fig. 1. A focused continuous-wave laser beam photogenerates a hot-carrier distribution in a limited region of a hot-carrier absorber. These carriers move away from the generation region under the influence of both concentration and temperature gradients. To account for this transport and quantify the corresponding transport coefficients, we derive a framework appropriate for hot-carrier solar cells.

A. Bipolar diffusion

In semiconductors, carrier diffusion is *bipolar*, as, in general, carriers in the conduction and valence bands must both be considered. In this work, we describe carriers in the valence band as holes. To treat holes as real quasiparticles, symmetrical to electrons in the conduction band, we consider that the hole energy is opposite to the energy of the corresponding electron in the valence band. This is represented schematically in Fig. 2, which defines the energy conventions used in this work.

Carrier diffusion is described through steady-state carrier conservation:

$$0 = \partial_t n_i = G_i - R_i - \nabla \cdot \mathbf{J}_{N,i}, \tag{2}$$

where the subscript i denotes either electrons (e) or holes (h). n_i is the concentration of the carrier i, G_i (R_i) is the generation (recombination) rate, and $J_{N,i}$ is the particle current. In the linear regime, this current is [25,27]

$$\mathbf{J}_{N,i} = \frac{\sigma_i}{q_i}\mathbf{E} - \frac{\sigma_i}{e^2}\nabla\mu_i - \frac{\sigma_i S_i}{q_i}\nabla T, \tag{3}$$

where σ_i is the electrical conductivity, S_i is the Seebeck coefficient, $q_i = \pm e$ is the algebraic charge, while $e = 1.6 \times 10^{-19}$ C is the absolute elementary charge, μ_i is the *chemical potential*, and $\mathbf{E}$ is the electrical field.

The electrical field has a contribution from (i) the possible external bias applied to the cell, and (ii) the local charge concentration through the Poisson equation. The latter contribution allows us to describe the interaction between electrons and holes. In this study, we consider the limiting case of a strong interaction: the ambipolar diffusion regime.

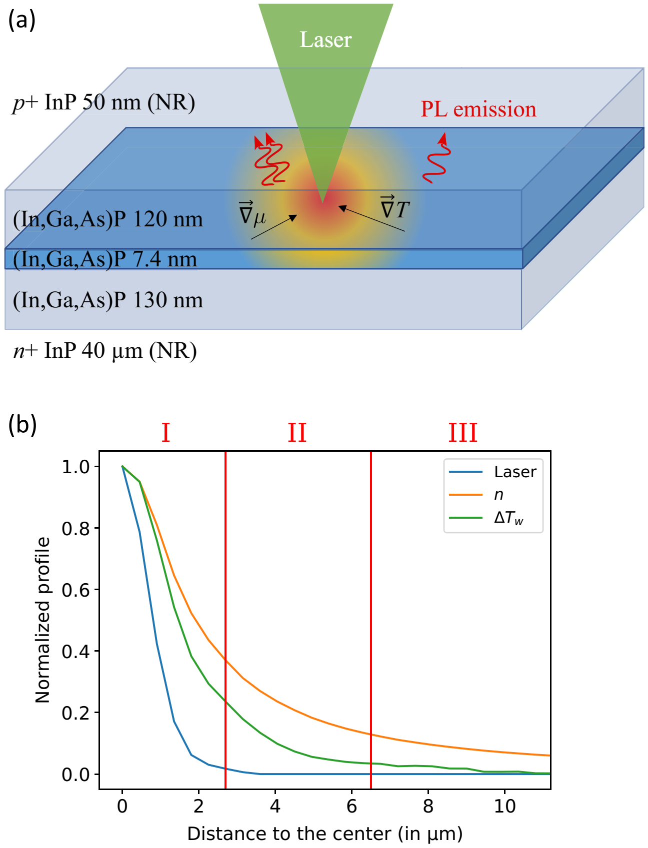

FIG. 1. (a) (In, Ga, As)P quantum well structure studied in this work and schematic of our method to determine the Seebeck coefficient from hyperspectral PL measurements. NR stands for “not represented.” (b) Normalized laser, carrier concentration, and temperature profiles measured at an excitation intensity of $I_{\text{exc}} = 5.7 \times 10^4$ W cm^{-2}. Vertical lines highlight three regimes: III, isothermal diffusion, where electrical conductivity may be measured; II, thermoelectric diffusion, where the Seebeck coefficient may be measured; I, region dominated by generation and not used in this study.

B. Ambipolar diffusion in the nondegenerate regime

In ambipolar diffusion, the electrostatic attraction between electrons and holes is strong enough to bind both populations. Therefore, the electron and hole particle currents are equal:

$$\mathbf{J}_{N,e} = \mathbf{J}_{N,h}. \tag{4}$$

In addition, generation and recombination processes are symmetrical for electrons and holes, i.e., $G_e = G_h$ and $R_e = R_h$. Finally, at high injection levels, we can assume that doping is negligible compared with photogenerated charge concentrations. The combination of these three

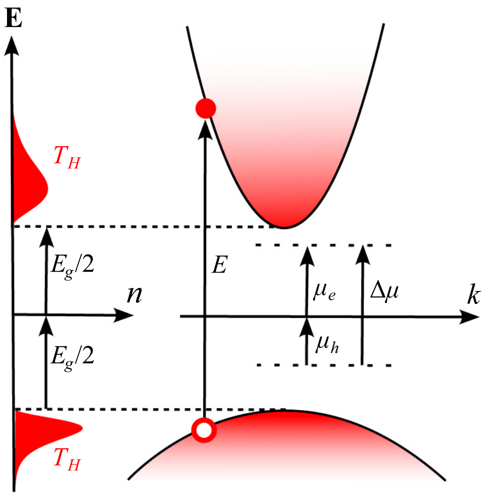

FIG. 2. Schematic of a hot-carrier absorber in the parabolic band approximation and energy conventions used in this work. Carrier densities are represented in the case where holes are heavier than electrons. Note that the chemical potential of holes (μ_h) is opposite that of electrons in the valence band ($\mu_{e,V}$), such that $\Delta\mu = \mu_e + \mu_h = \mu_{e,C} - \mu_{e,V}$.

effects implies that local electroneutrality must hold, such that $n_e(r) = n_h(r)$.

Note that the system investigated here is a quantum well, in which the well and the barrier may exchange carriers. This may disrupt the electroneutrality assumption. However, for this particular structure, the band-edge mismatch between the well and the barrier is almost the same for electrons and holes [11]. In addition, at the high carrier densities reached in the following experiment ($n \sim 10^{18}$ cm^{-3}), a discrepancy of carrier density would be prevented by the creation of a strong transverse electrical field. Therefore, we expect that electroneutrality holds in this case.

In the effective mass approximation, electroneutrality takes the following dimensionless form:

$$m_e^{D/2}\int_0^\infty \frac{x^{D/2-1}dx}{1+\exp\left(x+\frac{E_g/2-\mu_e}{k_BT}\right)} = m_h^{D/2}\int_0^\infty \frac{x^{D/2-1}dx}{1+\exp\left(x+\frac{E_g/2-\mu_h}{k_BT}\right)}, \tag{5}$$

where m_e (m_h) is the effective mass of electrons (holes), D is the dimensionality of the system, E_g is the band gap, and k_B is the Boltzmann constant. This relationship can be written in differential form:

$$\nabla\mu_h = g_1(\mu_e,\mu_h,T)\nabla\mu_e + g_2(\mu_e,\mu_h,T)\nabla T. \tag{6}$$

See Appendix D for details of the derivation of g_1 and g_2.

Using this simplification, one can evaluate the electrostatic field necessary to ensure that transport is ambipolar [Eq. (4)] [24]:

$$\mathbf{E} = \frac{1}{e}\frac{g_1\sigma_h - \sigma_e}{\sigma_e+\sigma_h}\nabla\mu_e + \left(\frac{\sigma_e S_e + \sigma_h S_h}{\sigma_e+\sigma_h} + \frac{\sigma_h}{\sigma_e+\sigma_h}\frac{g_2}{e}\right)\nabla T. \tag{7}$$

Note that we would find a similar expression with $\nabla\mu_h$.

Injecting this expression into Eq. (2), we find that the ambipolar hot-carrier current is

$$\mathbf{J}_{N,i} = -\frac{\sigma_{\mathrm{amb},i}}{e^2}\nabla\mu_i - \frac{\sigma_{\mathrm{amb},i}S_{\mathrm{amb},i}}{q_i}\nabla T, \tag{8}$$

where $\sigma_{\mathrm{amb},i}$ ($S_{\mathrm{amb},i}$) is the effective ambipolar electrical conductivity (Seebeck coefficient), defined as

$$\sigma_{\mathrm{amb},e} = \frac{\sigma_e\sigma_h}{\sigma_e+\sigma_h}(1+g_1),\quad \sigma_{\mathrm{amb},h} = \frac{\sigma_e\sigma_h}{\sigma_e+\sigma_h}(1+1/g_1),$$
$$S_{\mathrm{amb},e} = \frac{e(S_e-S_h)-g_2}{e(1+g_1)},\quad S_{\mathrm{amb},h} = \frac{e(S_h-S_e)-g_2/g_1}{e(1+1/g_1)}. \tag{9}$$

This is the main theoretical result of this work, which does not depend on the specificity of the experimental conditions. It shows that, in the context of hot-carrier solar cells, a full description of the ambipolar transport resembles the usual thermoelectric equations with effective ambipolar coefficients.

Note that, in our case, contrary to the textbook treatment of *homogeneous* thermoelectric transport [26], it is not possible to attribute one single ambipolar electrical conductivity nor one single ambipolar Seebeck coefficient to electrons and holes. This is a consequence of electroneutrality, which imposes the condition that electron and hole chemical potentials differ by a temperature-dependent term [see Eq. (6)].

III. HYPERSPECTRAL IMAGING OF CARRIER DISTRIBUTIONS

To measure transport coefficients defined in the previous section, we perform a hyperspectral PL measurement with a punctual illumination, as described in Fig. 1. This allows us to access temperature and QFLS profiles [28] required to compute the particle current.

A. Materials and methods

We use a 980-nm laser focused to a Gaussian profile with a radius of 1.6 μm at 2σ to generate hot carriers in a $\mathrm{In_{0.78}Ga_{0.22}As_{0.81}P_{0.19}/In_{0.8}Ga_{0.2}As_{0.435}P_{0.565}}$ single quantum well (QW). Further details regarding the sample are published in Ref. [11].

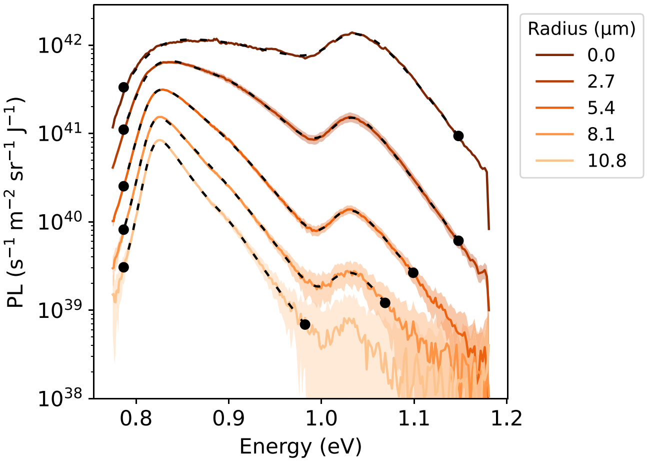

FIG. 3. Angularly integrated PL spectra obtained at different radii for a single excitation intensity of $I_{\text{exc}} = 4.1 \times 10^4$ W cm^{-2}. Pale envelope represents the dispersion of spectra aggregated during integration. Dashed lines represent the result of a full fit (see Appendix A).

PL emitted from the surface of the sample is collected using a near-infrared (NIR) hyperspectral imager equipped with a Mitutoyo APO NIR ×50 objective lens (0.41 NA). It has a spatial resolution (sparrow criterion) of 1.7 μm and a spectral resolution of 2 nm. Taking advantage of the cylindrical symmetry of the problem, we integrate angularly to obtain PL spectra as a function of the distance from the laser spot (up until ∼13 μm) for different central laser intensities ranging from 6.3×10^3 to 2.3×10^5 W cm^{-2}. Our dataset is therefore composed of 270 PL spectra, corresponding to hyperspectral acquisitions at nine different excitation intensities and 30 different radii (from 0 to 13 μm) for each intensity.

A few PL spectra collected at different radii are reported in Fig. 3. The peak around 0.82 eV is attributed to the emission of the quantum well, while the peak at 1.05 eV is consistent with emission from the barrier [11]. The shape of the quantum well emission spectrum depends strongly on the distance to the laser, which is indicative of a stronger hot-carrier effect and band-filling effect in the center.

B. Hot-carrier spectroscopy

We probe local carrier distributions by analyzing the local PL emission. According to the generalized Planck law [29], the PL spectrum is related to the carrier temperature and chemical potential by

$$I_{\text{PL}}(E) = \frac{2}{h^3c^2} A(E, \Delta\mu, T) \frac{E^2}{\exp\left(\frac{E-\Delta\mu}{k_BT}\right) - 1}, \tag{10}$$

where I_{PL} is the emitted flux in s^{-1} m^{-2} sr^{-1} J^{-1}, A is the sample absorptivity (which may include population-dependent effects, see Appendix A), $\Delta\mu$ is the QFLS, T is the carrier temperature, h is Planck's constant, and c is the speed of light in a vacuum.

Estimating carrier distribution from a PL spectrum requires absolute calibration of the setup and good knowledge of the absorptivity to perform a full fit of the spectra [11]. An example of this full-fit analysis is shown in Fig. 3. Such advanced fitting methodologies are particularly critical in the context of hot carriers in nanostructures, where the strong excitation regime leads to a significant band filling [30,31]. Details of the full-fit model are presented in Appendices A and B.

The uncertainty on the determination of the absorption coefficient (see Appendix B) leads to an estimated ±20 meV uncertainty in the QFLS. Additionally, noise in the PL spectra and partial overfitting introduce a random uncertainty of approximately 1% for both variables.

To distinguish hot carriers from the laser-induced heating of the sample, we assess the lattice temperature by monitoring the PL peak according to Varshni's law [32]. The absence of a peak shift indicates that the lattice remains at ambient temperature, while carriers can reach temperatures higher than 1000 K (see Fig. 4).

C. Carrier-distribution profiles

From the measurement of $T(r)$ and $\Delta\mu(r)$, and owing to local electroneutrality, we deduce the local carrier density, $n(r) = n_e = n_h$, and the corresponding chemical potentials $\mu_e(r)$ and $\mu_h(r)$. These measurements are all reported in Fig. 4. Note that carrier density and chemical potentials are computed using Fermi-Dirac distributions.

Figure 4(a) shows the spatial distribution of the carrier temperature for increasing laser intensities. Temperature is shown to increase with increasing excitation intensity, as we expect from a hot-carrier absorber [33]—except for a few incoherent spectra at highest intensity and close to the center. In this range of power, the carrier temperature reaches more than 1000 K. It is also shown to decrease as we look further and further away from the center. At distances larger than 10 μm, carriers are thermalized with the lattice at room temperature, regardless of the excitation intensity.

At high excitation intensities, the carrier temperature remains above room temperature for typically 6–8 μm, much larger than the laser radius. Therefore, we report a hot-carrier diffusion length in the order of a few μm, several times the value previously reported in monolayers (∼500 nm) [34,35], in perovskite thin films (∼230 nm) [36], and in nanowires (∼300 nm) [37].

Carrier-density profiles are presented in Fig. 4(b). Carrier density is increasing with increasing excitation intensity, as absorbing more photons will promote more carriers in the bands. Additionally, carrier density decreases with increasing distance to the center. This is expected from a

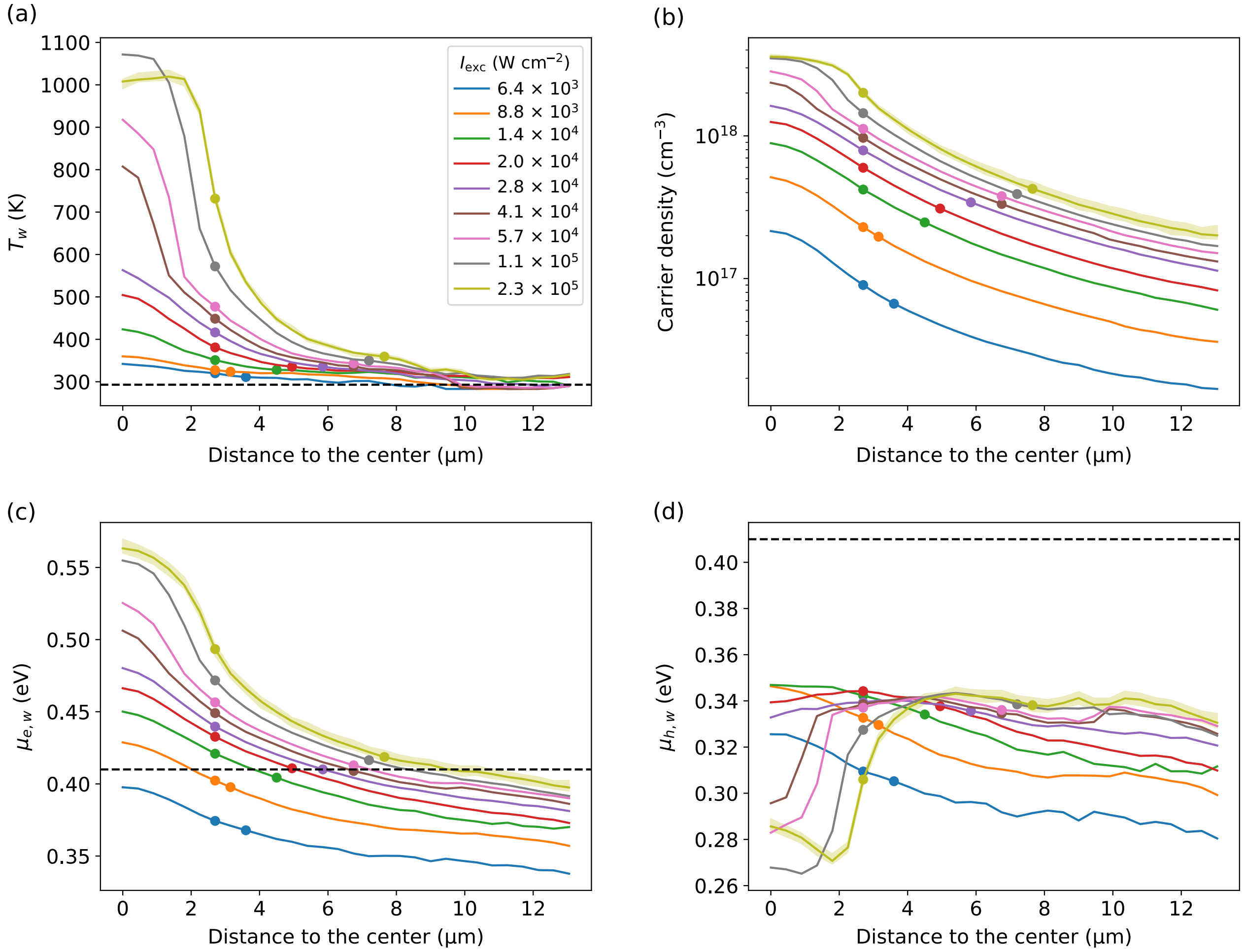

FIG. 4. (a) Estimated carrier-temperature profile in the quantum well at all excitation intensities. (b) Carrier density estimated from PL measurements. Dashed line indicates room temperature, $T_{\rm amb} = 293$ K. Chemical potential of (c) electrons and (d) holes in the quantum well. Dashed line represents the electron (hole) band edge. Dots represent the boundaries of region II defined in Fig. 1 and Sec. IV. Pale-green region indicates the estimated error bars (Sec. III B) for the highest excitation intensity. Similar error bars are expected at all intensities but are not represented to enhance readability.

punctual illumination experiment, as carriers are photogenerated at the center, and then diffuse to further distances while recombining. Note that in exotic cases with strong enough thermoelectric transport, it is possible to observe a depletion of carrier density close to the center [18]. Such an effect did not occur in our experiment.

Electron (hole) chemical potential profiles are presented in Fig. 4(c) [Fig. 4(d)]. At high excitation intensities, the electrons form a completely degenerate electron gas, as their chemical potential is well above the conduction band ($E_C \simeq 0.41$ eV). However, the hole distribution remains nondegenerate due to the discrepancy in effective masses. Surprisingly, at high intensity, the hole chemical potential decreases as we come closer to the center. This can be explained by the large increase of carrier temperature in this region. Therefore, despite the drop of chemical potential, carrier density is still increasing when we go closer to the center [see Fig. 4(b)].

IV. AMBIPOLAR TRANSPORT COEFFICIENTS DETERMINED BY PHOTOLUMINESCENCE

In the ambipolar configuration, electrons and holes diffuse at the same rate, such that it is equivalent to study one or the other. In this section, we choose to study electrons, and we distinguish three different spatial regions (see Fig. 1).

In the central region (I), close to the laser beam, the generation term is significant in the continuity equation [Eq. (2)]. We estimate that this region spans until the laser intensity reaches 5% of its maximal intensity, namely, $r = 2.7$ µm. In a complex stack such as this quantum well, obtaining a precise estimate of the generation rate is not easy. Therefore, we simply discard this region.

Far from the center (III; typically 3.6–7.7 µm), carriers have relaxed towards the lattice temperature. In this region, the concentration profile is determined by isothermal diffusion. This allows us to measure the *electrical conductivity*.

In between these regions (II), carriers experience a significant temperature gradient. Therefore, their transport is induced not only by the charge-concentration gradient but also by thermoelectric effects. This region grants access to the *Seebeck coefficient*.

The boundaries of these three regions are represented for every excitation intensity in Fig. 4.

A. Determination of the electrical conductivity

In region III, the continuity equation is simplified by the absence of generation and of a temperature gradient. In this context, the only terms left in this equation are the isothermal diffusion term and the recombination term, and Eq. (2) becomes $R = \nabla \cdot \left(\sigma_{\mathrm{amb},e}/e^2 \times \nabla\mu_e\right)$.

The electrical conductivity can be written in terms of carrier mobilities, $\bar{\mu}_i$, as $\sigma_{\mathrm{amb},e} = \gamma_e(1+g_1)n$, where we introduce the parameter $\gamma_e = e\bar{\mu}_e\bar{\mu}_h/(\bar{\mu}_h - \bar{\mu}_e)$. By assuming that carrier mobilities are constant, and noticing that g_1 slowly varies with the position, we can take the factor $\gamma_e(1+g_1)$ out of the gradient in the equation above.

To measure the conductivity, we need an estimate of the recombination rate. In this study, carrier density is around 10^{18} cm^{-3} [see Fig. 4(b)], such that we assume that the recombination rate is dominated by the Auger process, $R = Cn^3$ (see Appendix C for details). Therefore, in the isothermal region, Eq. (2) becomes

$$\frac{C}{\gamma_e} = \frac{1+g_1}{n^3}\nabla \cdot \left(\frac{n}{e^2}\nabla\mu_i\right). \tag{11}$$

The determination of the Auger scattering rate, C, is beyond the scope of this article [38]. Therefore, we can only access the ratio C/γ_e and estimate the electrical conductivity up to a multiplicative constant. We find that the ratio of C/γ_e decreases with increasing excitation intensity and has a typical order of magnitude of 10^{-22}–10^{-20} m^4 V s^{-1} A^{-1}. This is consistent with typical values of the Auger coefficient in (In, Ga, As)P quantum wells, $C \sim 10^{-27}$ cm^6 s^{-1} [39], and mobility $\bar{\mu}_e \sim 10^{3-4}$ cm^2 (V s)$^{-1}$ [38].

Note that, due to noise on the determination of the right-hand side of Eq. (11), fitted values of C/γ_e have a typical uncertainty of ±15%.

B. Determination of the Seebeck coefficient

1. Computation

We now turn to the analysis of region II. We assume that the variations of $S_{\mathrm{amb},e}$ are sufficiently small, such that the contribution of $\nabla S_{\mathrm{amb},e}$ to transport is negligible. Under this assumption, Eq. (2) can be rewritten to express the ambipolar Seebeck coefficient from measured quantities as

$$S_{\mathrm{amb},e} \simeq -\frac{-\frac{C}{\gamma_e}n^3 + \frac{1+g_1}{q_e^2}\nabla\left(n\cdot\nabla\mu_e\right)}{\frac{1}{q_e}\nabla\left(n\cdot\nabla T\right)}, \tag{12}$$

where the quantity C/γ_e has been estimated from Eq. (11).

To compute uncertainty on this ambipolar Seebeck coefficient, we consider the following error sources: (i) random noise on the temperature profiles; (ii) random shift of the QFLS profiles, as explained in Sec. III B; and (iii) an uncertainty on the estimate of C/γ_e, as explained in Sec. IV A.

2. Results and qualitative discussion

Experimental determination of the ambipolar Seebeck coefficient under all relevant excitation conditions is presented in Fig. 5. The ambipolar Seebeck coefficient takes values between −4 and $1k_B/e$, which is the typical order of magnitude of Seebeck coefficients in QWs [40]. Points with an uncertainty larger than $4k_B/e$ are not represented.

Such a large value is surprising, however, for an *ambipolar* Seebeck coefficient. This is because the usual derivation of an ambipolar Seebeck coefficient is done under *dark conditions* and leads to $S_{\mathrm{amb}} = (\sigma_e S_e + \sigma_h S_h)/(\sigma_e + \sigma_h)$ [26]. In such cases, the Seebeck coefficients of electrons and holes compensate for each other. However, this article addresses the case of *strong photogeneration*, and therefore, our ambipolar Seebeck coefficient is different in nature. In our case, Seebeck coefficients of electrons and holes *add up*, as shown in Eq. (9). Therefore, we expect that our ambipolar Seebeck coefficient should be of the same order of magnitude as those of electrons and holes.

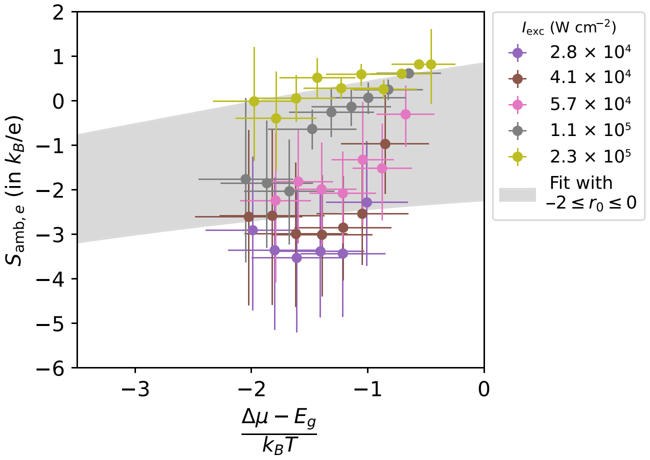

FIG. 5. $S_{\mathrm{amb},e}$ obtained from Eq. (12) plotted versus the corresponding reduced QFLS, $\eta = (\Delta\mu - E_g)/k_BT$, deduced from PL measurements. Gray region indicates the values modeled from the Boltzmann transport equation [see Eq. (13)] with $-2 \leq r_0 \leq 0$.

3. Comparison with the Boltzmann transport equation

For a more quantitative discussion, we make use of the Boltzmann transport equation in the relaxation-time approximation. This theory provides a model for the Seebeck coefficient of a gas of particles with charge q_i [41]:

$$S_i = -\frac{1}{q_i T}\left[\mu_i - \frac{E_g}{2} - \frac{\int_0^\infty D_i(\epsilon)\epsilon^{r_0+2}\frac{\partial f_i}{\partial \epsilon}d\epsilon}{\int_0^\infty D_i(\epsilon)\epsilon^{r_0+1}\frac{\partial f_i}{\partial \epsilon}d\epsilon}\right], \qquad (13)$$

where $\mu_i - E_g/2$ is the difference between the chemical potential of carrier i and its band edge (see Fig. 2), $\epsilon = E - E_g/2$ is the kinetic energy, D_i is the density of state, f_i is the occupation function (Fermi-Dirac in this case), and $\tau(\epsilon) \propto \epsilon^{r_0}$ is a standard parametrization of the relaxation time. We assume that r_0 is the same for electrons and holes. From this equation, the ambipolar Seebeck coefficient can be computed with Eq. (9). Note that in this approach, the ambipolar Seebeck coefficient, $S_{\mathrm{amb},e}$, is parametrized by one single free parameter: r_0.

Because of the dispersion on our data, it is not possible to determine an exact value for r_0. However, our measured values of the ambipolar Seebeck coefficient are consistent with $-2 \leq r_0 \leq 0$ (see Fig. 5). This confirms that our method allows us to measure meaningful ambipolar Seebeck coefficients.

The comparison of our results with the Boltzmann transport equation also allows us to study the asymptotic behavior of the ambipolar Seebeck coefficient. In the nondegenerate regime, $\Delta\mu \ll E_g - k_BT$ (i.e., $\eta \ll -1$), Eq. (13) predicts that $S_{\mathrm{amb},e} = k_B/2e \times [\eta - (r_0 + 2) + \ln(m_h/m_e)]$ is linear in the reduced QFLS with a universal slope of $k_B/2e$ [26]. This means, in particular, that the ambipolar Seebeck coefficient should be larger at lower η, and hence, for lower excitation intensity, as is the case with photo-Seebeck [23]. However, if the excitation is not high enough, carriers will stay cold and our optical method will not allow us to measure the Seebeck coefficient. In this study for instance, acquisitions with intensity $I_{\mathrm{exc}} < 2 \times 10^4$ W cm^{-2} did not exhibit large enough temperature variations to allow for a precise determination of $S_{\mathrm{amb},e}$; thus, they are not reported in Fig. 5.

In the degenerate regime, Eq. (13) predicts that $S_i = \pi^2 k_B(r_0 + 1)/3q_i\eta$, which tends to 0 as $\eta \to \infty$. In this regime, $S_{\mathrm{amb},e} \simeq -g_2/(1 + g_1)$ has no clear asymptotic behavior (see Fig. 9).

Note also that the ambipolar Seebeck coefficient depends directly on the ratio of the electron and hole effective masses, m_h/m_e, through g_1 and g_2 (see Appendix D and Fig. 9). To achieve a large negative $S_{\mathrm{amb},e}$, we should seek materials with m_h/m_e as low as possible. However, we should keep in mind that a large negative S will result in a small positive $S_{\mathrm{amb},h}$ and vice versa, as shown by Eq. (9) and Fig. 9.

V. CONCLUSION

This article lays the theoretical framework necessary to study the thermoelectric ambipolar transport of photogenerated hot carriers. We described this transport with effective ambipolar transport coefficients that were valid even in the degenerate case. We proposed a purely optical method to measure these coefficients. It relied on the use of absolutely calibrated hyperspectral photoluminescence. We validated this method by determining the ambipolar transport coefficients—and in particular the Seebeck coefficient—in an (In, Ga, As)P quantum well. Results were shown to be consistent with the Boltzmann transport equation in the relaxation-time approximation.

This study opens different perspectives to understand the properties of nonideal hot-carrier solar cells, where transport phenomena may limit device efficiency. Specifically, it enables the description of inhomogeneous hot-carrier solar cells, where carrier transport is influenced by inhomogeneous hot-carrier distributions.

ACKNOWLEDGMENTS

The authors would like to acknowledge the French National Research Agency, specifically the grant ANR ICEMAN 19-CE05-0019-01, as well as the PEARL program of IPVF for providing funds for this research. We especially thank the FOTON Institute for providing the sample. The authors also thank Christophe Goupil and Stanko Tomic for valuable discussions over the course of the project.

APPENDIX A: DESCRIPTION OF THE PHOTOLUMINESCENCE MODEL

In this appendix, we describe the model used to describe and fit our PL spectra. In the generalized Planck law, most of the difficulties in term of modeling come from the absorptivity, A, which depends on many variables.

1. Description of a single layer

a. Absorptivity and absorption coefficient

If we neglect reflections at the different interfaces, the absorptivity, A, of a single layer of thickness d can be linked to its coefficient of absorption, α, by the Beer-Lambert law:

$$A = (1 - R(E))\,(1 - \exp(-\alpha d))\,. \qquad (A1)$$

The absorption coefficient itself depends both on material parameters (band structure, defect densities, etc.) and on carrier distribution through the effect commonly called “band filling” (or the “Moss-Burnstein effect”) [42]. Other effects such as band-gap renormalization and changes in reflectivity are disregarded here. Therefore, we write

$$\alpha(E) = \alpha_0(E) \times BF(E, \Delta\mu, T), \tag{A2}$$

where α_0 is the absorptivity coefficient measured in the dark, and $BF = 1 - f_h - f_e$ is the contribution of band filling. Here, we explicitly write the dependence of BF on the carrier distribution, but it also depends on the band structure of the material. In an effective-mass model only including contributions from the Γ valley, one can show that [11]

$$BF(E, \Delta\mu, T) = \frac{\sinh\left(\frac{E-\Delta\mu}{2k_BT}\right)}{\cosh\left(\frac{E-\Delta\mu}{2k_BT}\right) + \cosh\left[\frac{m_h-m_e}{m_h+m_e}\frac{E-E_g}{2k_BT} - \frac{D}{4}\ln\frac{N_V}{N_C}\right]}, \tag{A3}$$

where E_g is the band gap of the considered material, m_i is the effective mass of particle i, and D is the dimensionality of the considered layer. In our case, $D = 2$ for the quantum well and $D = 3$ for the barrier.

Because we measured QFLS values close to the band gap for both the quantum well and the barriers, we included this band-filling contribution in the absorption of both layers. We consider that, in the quantum well, $m_{e,w} = 0.042m_0$ and $m_{h,w} = 0.41m_0$, while, in the barrier, $m_{e,b} = 0.061m_0$ and $m_{h,b} = 0.54m_0$ [11]. $m_0 = 9.1 \times 10^{-31}$ kg is the mass of one electron.

b. Quantum well emission

Quantum wells have a steplike density of states, and therefore, steplike absorptivity. In our case, two levels seem sufficient to explain our PL spectra. It has been shown that exciton states may also have a significant contribution at room temperature [43,44]. Therefore, we model our quantum well absorptivity with nine parameters (A_x, E_x, Γ_x, A_1, R_y, Γ_1, A_2, E_2, Γ_2):

$$\begin{aligned}\alpha_0^{\mathrm{QW}} &= A_x \exp\left[-\left(\frac{E-E_x}{\Gamma_x}\right)^2\right] + A_1\frac{1}{1+\exp\left[-\left(\frac{E-E_1}{\Gamma_1}\right)\right]}\\ &\quad\times \frac{2}{1+\exp\left(-2\pi\sqrt{\frac{R_y}{|E-E_1|}}\right)}\\ &\quad + A_2\frac{1}{1+\exp\left[-\left(\frac{E-E_2}{\Gamma_2}\right)\right]},\end{aligned} \tag{A4}$$

where E_i denotes the position of energy level i, A_i is the amplitude of the transition, and Γ_i is a broadening parameter. $R_y = E_1 - E_x$ is the Rydberg binding energy of excitons. Note that we took into account the Sommerfeld enhancement factor in the emission of the first level.

c. Barrier emission

For the absorptivity of the barrier layer, we use a phenomenological steplike absorption:

$$\alpha_0^B = A_b\frac{1}{1+\exp\left(-\frac{E-E_b}{\Gamma_b}\right)}. \tag{A5}$$

Note that it is not necessary to use a more advanced model for the barrier because we are solely interested in the carrier distribution *in the quantum well*, which is only weakly affected by the model used for the barrier emission.

2. Emission of a multilayer

In a multilayer, light emitted in a deep layer may be partially reabsorbed by shallower layers. By denoting A_w (A_b) the absorptivity of the quantum well (barrier), we can write [11]

$$\begin{aligned}I_{\mathrm{PL}}(E) = \frac{2E^2}{h^3c^2}\Bigg\{&\frac{A_w(1-A_b)}{\exp\left(\frac{E-\Delta\mu_w}{k_BT_w}\right)-1}\\ &+\frac{A_b(1-A_w)(1-A_b)+A_b}{\exp\left(\frac{E-\Delta\mu_b}{k_BT_b}\right)-1}\Bigg\}.\end{aligned} \tag{A6}$$

APPENDIX B: FITTING METHODOLOGY

In total, our full-fit model includes 16 parameters. Four are related to the carrier distribution in the well (T_w, $\Delta\mu_w$) and in the barrier (T_b, $\Delta\mu_b$), and 12 are related to the material (A_x, E_x, Γ_x, A_1, R_y, Γ_1, A_2, E_2, Γ_2, A_b, E_b, Γ_b). These 16 parameters are partially redundant, so we need a strategy to reduce the risk of overfitting our data and obtain meaningful values for the carrier-distribution parameters that we are most interested in.

For the band-to-band transition, some of the material parameters remain constant when changing the excitation intensity. This is the case for the absorption amplitudes (A_1, A_2, A_b) and the energies of the optical transition (E_x, R_y, E_2, E_b). However, the linewidths (Γ_x, Γ_1, Γ_2, Γ_b) are power dependent because they depend on the phonon density [31]. Similarly, the contribution of the excitonic transition, A_x, can be screened by increasing carrier density [43].

External quantum efficiency (EQE) measurements can be used to determine the low-power absorptivity, $A = (1 - R)(1 - \exp(-\alpha_0 d))$. Indeed, assuming that all photogenerated carriers are extracted in the contacts, the EQE spectrum equals the absorptivity.

Figure 6 shows the EQE spectrum measured with a ThermoFisher FTIR-FTPS instrument using a resolution of 32 cm^{-1}. It was fitted against an absorptivity model derived from Eq. (A6), assuming that $T_w = T_b = 293$ K and $\Delta\mu_w = \Delta\mu_b \ll E_x$. As explained above, seven of

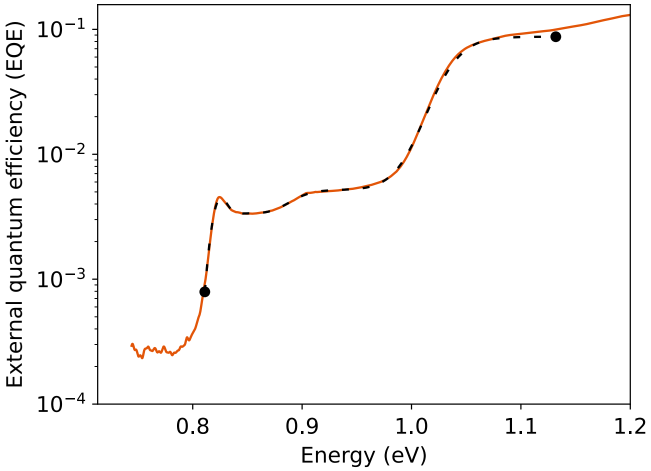

FIG. 6. EQE spectrum obtained at room temperature, along with a fit using the absorptivity model described in the text.

the 12 fitted parameters are only *material dependent* and should not depend on the excitation condition. Table I reports the fitted values of these parameters, which are used to model all PL spectra.

Five more *power-dependent* parameters are necessary to reproduce the EQE spectrum, and are reported in Table II. These parameters depend on excitation intensity and on position, such that they are kept as fitting parameters for the PL spectra [11].

To summarize, fitting the EQE spectrum allowed us to determine seven parameters prior to fitting PL spectra. Only nine parameters were left to fit for each PL spectrum (T_w, $\Delta\mu_w$, T_b, $\Delta\mu_b$, A_x, Γ_x, Γ_1, Γ_2, Γ_b). We used a differential evolution algorithm [45] to search for the global minimum in this parameter space with nine dimensions. We used an objective function on the $\log_{10}$ scale, as our PL spectra cover several orders of magnitude.

APPENDIX C: ASSESSING THE STRENGTH OF AUGER RECOMBINATIONS

In this appendix, we explain in detail why Auger recombination is considered dominant in our study.

First, we measure high carrier densities, $n \sim 10^{18}$ cm^{-3}, even far from the center [see Fig. 3(d)]. Assuming an Auger coefficient of $C \sim 10^{-27}$ [39], we get an Auger recombination rate of $Cn^3 \sim 10^{27}$ cm^3 s^{-1}, which is comparable to or higher than monomolecular recombination rate $R = n/\tau$, assuming a carrier lifetime of $\tau \sim 1$ ns.

TABLE I. Absorption parameters determined by EQE measurements. Absorption coefficients are in m^{-1} while energies are in eV. These values are used to fit all PL spectra in this study.

Parameter	E_x	A_1	E_1	A_2	E_2	A_b	E_b
Value	0.823	5.4 10^5	0.808	7.4 10^5	0.890	8.5 10^5	1.035

TABLE II. Power-dependent absorption parameters necessary to reproduce the EQE spectrum. Absorption coefficients are in m^{-1} while spectral bandwidth are in eV. These parameters were fitted again for each and every PL spectrum presented in the main text, as they depend on carrier population.

Parameter	A_x	Γ_x	Γ_1	Γ_2	Γ_b
Value	6.5 10^5	0.007	0.005	0.011	0.013

Second, by modeling transport far from the center, we show that the measured profiles of carrier density and chemical potential can be best explained by Auger recombinations. Far from the center, generation is negligible and carriers are thermalized such that the recombination rate must balance the isothermal particle current: $R = (1/e^2)\nabla \cdot (\sigma \nabla \mu_e)$ (see main text Sec. IV A). Figure 7 compares these two quantities using three different scalings for the recombination rate: monomolecular ($R = n/\tau$), bimolecular ($R = Bn^2$), and Auger ($R = Cn^3$). One sees that Auger recombination is the one that compensates for isothermal particle current the best at large distances.

APPENDIX D: DETAILS OF ELECTRONEUTRALITY AND THE DERIVATION OF g_1 AND g_2

In the effective-mass approximation, assuming a typical density of states, $D_i(\epsilon) \propto m_i^{D/2}\epsilon^{D/2-1}$, electroneutrality takes the following form:

$$m_e^{D/2}\int_0^\infty h(x,\mu_e,T)dx = m_h^{D/2}\int_0^\infty h(x,\mu_h,T)dx, \quad \text{(D1)}$$

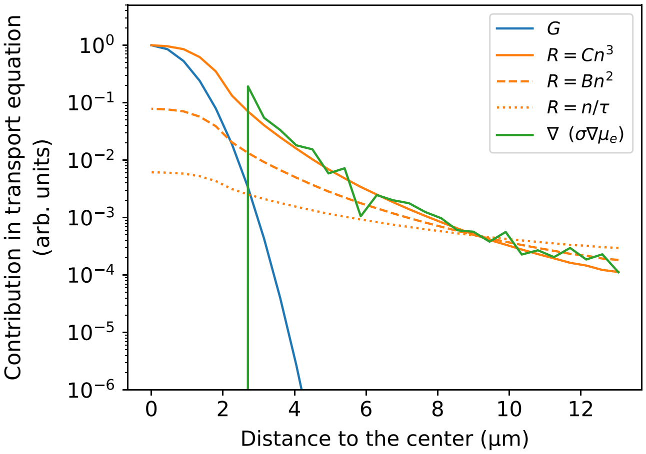

FIG. 7. Contribution of the different terms in the transport equation [Eq. (2)] in the isothermal regime, assuming various dominant recombination mechanisms (monomolecular, bimolecular, or Auger). Far from the center, carrier conservation means that yellow and green lines should compensate for each other. Profiles are established based on a high intensity acquisition ($I_{\rm exc} = 1.1 \times 10^5$ W cm^{-2}).

where we introduce the function

$$h(x,\mu,T) = x^{D/2-1} \Big/ \left(1+\exp\left(x+\frac{E_g/2-\mu}{k_B T}\right)\right). \tag{D2}$$

Electroneutrality can be rewritten in the following differential form:

$$\nabla\mu_h = g_1(\mu_e,\mu_h,T)\nabla\mu_e + g_2(\mu_e,\mu_h,T)\nabla T, \tag{D3}$$

where

$$\begin{aligned} g_1(\mu_e,\mu_h,T) &= \left(\frac{m_e}{m_h}\right)^{D/2}\left(\int_0^\infty \frac{\partial h}{\partial\mu}(x,\mu_e,T)dx\right)\Big/\left(\int_0^\infty \frac{\partial h}{\partial\mu}(x,\mu_h,T)dx\right),\\ g_2(\mu_e,\mu_h,T) &= \left[m_e^{D/2}\int_0^\infty \frac{\partial h}{\partial T}(x,\mu_e,T)dx - m_h^{D/2}\int_0^\infty \frac{\partial h}{\partial T}(x,\mu_h,T)dx\right]\Big/\left[m_h^{D/2}\int_0^\infty \frac{\partial h}{\partial\mu}(x,\mu_h,T)dx\right]. \end{aligned} \tag{D4}$$

In the general case, these equations can only be computed numerically. Since PL measurements allow us to measure μ_e, μ_h, and T (see the main text), we can estimate these functions for all relevant experimental conditions. In the simpler case of a nondegenerate system, $h(x,\mu,T) \simeq x^{D/2-1}\exp(-x)\exp\left[(\mu-E_g/2)/k_B T\right]$ and electroneutrality takes the form

$$\mu_h = \mu_e - k_B T\frac{D}{2}\ln\left(\frac{m_h}{m_e}\right), \tag{D5}$$

such that

$$\begin{aligned} g_1 &= 1,\\ g_2 &= -k_B\frac{D}{2}\ln\left(\frac{m_h}{m_e}\right). \end{aligned} \tag{D6}$$

Figure 8 represents the values of g_1 and g_2 for varying reduced QFLS $\eta = (\Delta\mu - E_g)/k_B T$ and different values of mass mismatch, m_h/m_e. First, in the case $m_e = m_h$, we find that $\mu_e = \mu_h$, i.e., $g_1 = 1$ and $g_2 = 0$. Otherwise, it appears that, for all values of η, g_2 decreases with increasing mass mismatch, m_h/m_e. Note that in the nondegenerate regime ($\eta \ll -1$), $\mu_e = \mu_h + k_B T(D/2)\ln(m_h/m_e)$ [46], such that $g_1 = 1$ and $g_2 = -k_B(D/2)\ln(m_h/m_e)$.

From here, it is possible to compute the expected values of $S_{\mathrm{amb},e}$ and $S_{\mathrm{amb},h}$, as predicted from the Boltzmann transport equation [by combining Eqs. (9), (13) and (D4)]. These values are reported in Fig. 9. Notice how both $S_{\mathrm{amb},e}$ and $S_{\mathrm{amb},h}$ increase with the mass mismatch, m_h/m_e.

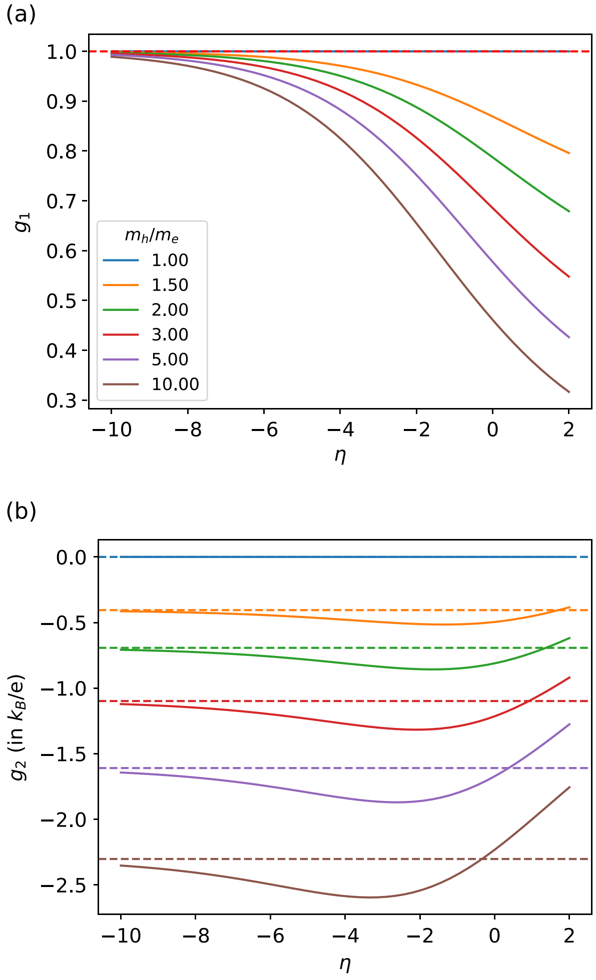

FIG. 8. (a) g_1 and (b) g_2 computed as a function of $\eta = (\Delta\mu - E_g)/k_B T$ for different mass mismatches, m_e/m_h, and assuming $T = 300$ K. Dashed lines represent the asymptotes in the nondegenerate case ($\eta \ll -1$).

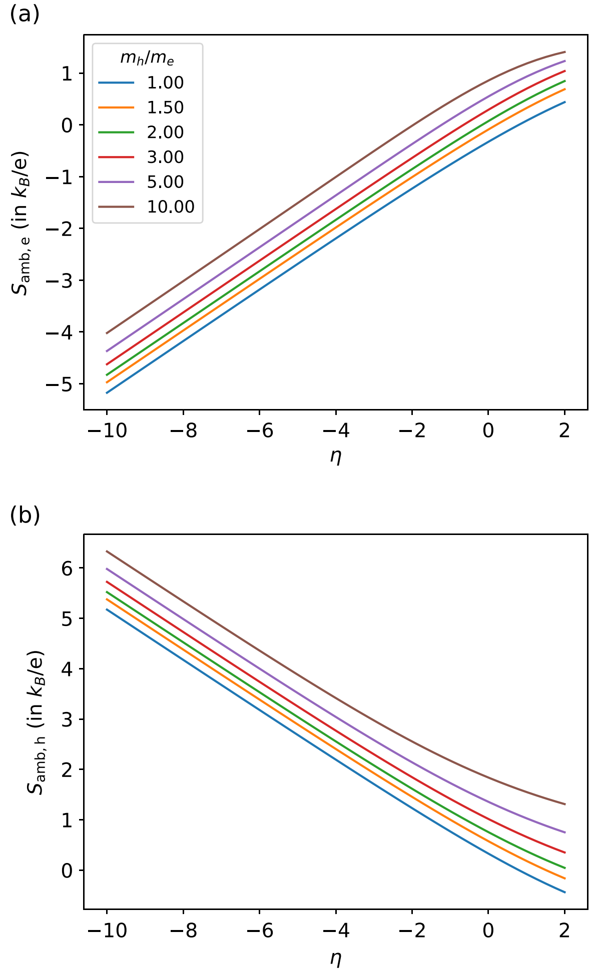

FIG. 9. (a) $S_{\mathrm{amb},e}$ and (b) $S_{\mathrm{amb},h}$ computed from the Boltzmann transport equation for different mass mismatches, m_e/m_h. We assume $T = 300$ K and $r_0 = -2$.

[1] J. Shah and R. C. C. Leite, Radiative recombination from photoexcited hot carriers in GaAs, Phys. Rev. Lett. **22**, 1304 (1969).

[2] Y. Rosenwaks, M. C. Hanna, D. H. Levi, D. M. Szmyd, R. K. Ahrenkiel, and A. J. Nozik, Hot-carrier cooling in GaAs: Quantum wells versus bulk, Phys. Rev. B **48**, 14675 (1993).

[3] C.-Y. Tsai, Theoretical model and simulation of carrier heating with effects of nonequilibrium hot phonons in semiconductor photovoltaic devices, Prog. Photovolt.: Res. Appl. **26**, 808 (2018).

[4] A. Othonos, Probing ultrafast carrier and phonon dynamics in semiconductors, J. Appl. Phys. **83**, 1789 (1998).

[5] B. Guzelturk, *et al.*, Nonequilibrium thermodynamics of colloidal gold nanocrystals monitored by ultrafast electron diffraction and optical scattering microscopy, ACS Nano **14**, 4792 (2020).

[6] Y. Takeda, S. Sato, and T. Morikawa, Hot-carrier photocatalysts for artificial photosynthesis, J. Chem. Phys. **156**, 164705 (2022).

[7] R. T. Ross and A. J. Nozik, Efficiency of hot carrier solar energy converters, J. Appl. Phys. **53**, 3813 (1982).

[8] P. Wurfel, Solar energy conversion with hot electrons from impact ionisation, Solar Energy Mater. Solar Cells **46**, 43 (1997).

[9] M. A. Green, in *Third Generation Photovoltaics: Advanced Solar Energy Conversion*, Springer Series in Photonics (Springer, Berlin, Heidelberg, 2003), p. 69.

[10] J. A. R. Dimmock, S. Day, M. Kauer, K. Smith, and J. Heffernan, Demonstration of a hot-carrier photovoltaic cell, Prog. Photovolt.: Res. Appl. **22**, 151 (2014).

[11] D.-T. Nguyen, L. Lombez, F. Gibelli, S. Boyer-Richard, A. Le Corre, O. Durand, and J.-F. Guillemoles, Quantitative experimental assessment of hot carrier-enhanced solar cells at room temperature, Nat. Energy **3**, 236 (2018).

[12] J. Rodiere, L. Lombez, A. Le Corre, O. Durand, and J.-F. Guillemoles, Experimental evidence of hot carriers solar cell operation in multi-quantum wells heterostructures, Appl. Phys. Lett. **106**, 183901 (2015).

[13] I. Konovalov and V. Emelianov, Hot carrier solar cell as thermoelectric device, Energy Sci. Eng. **5**, 113 (2017).

[14] A. Marti, E. Antolin, and I. Ramiro, Thermodynamics of the monoenergetic energy-selective contacts of a hot-carrier solar cell, Phys. Rev. Appl. **18**, 064048 (2022).

[15] L. Tesser, R. S. Whitney, and J. Splettstoesser, Thermodynamic performance of hot-carrier solar cells: A quantum transport model, Phys. Rev. Appl. **19**, 044038 (2023).

[16] F. Gibelli, L. Lombez, J. Rodiere, and J.-F. Guillemoles, Optical imaging of light-induced thermopower in semiconductors, Phys. Rev. Appl. **5**, 024005 (2016).

[17] S. Limpert, A. Burke, I.-J. Chen, N. Anttu, S. Lehmann, S. Fahlvik, S. Bremner, G. Conibeer, C. Thelander, M.-E. Pistol, and H. Linke, Bipolar photothermoelectric effect across energy filters in single nanowires, Nano Lett. **17**, 4055 (2017).

[18] S. Park, B. Han, C. Boule, D. Paget, A. Rowe, F. Sirotti, T. Taniguchi, K. Watanabe, C. Robert, L. Lombez, B. Urbaszek, X. Marie, and F. Cadiz, Imaging Seebeck drift of excitons and trions in MoSe$_2$ monolayers, 2D Mater. **8**, 045014 (2021).

[19] L.-L. Chao, G. S. Cargill, E. Snoeks, T. Marshall, J. Petruzzello, and M. Pashley, Diffusion lengths of excited carriers in Cd$_x$Zn$_{1-x}$Se quantum wells, Appl. Phys. Lett. **74**, 741 (1999).

[20] H. Zhao, S. Moehl, S. Wachter, and H. Kalt, Hot exciton transport in ZnSe quantum wells, Appl. Phys. Lett. **80**, 1391 (2002).

[21] B. A. Ruzicka, L. K. Werake, H. Samassekou, and H. Zhao, Ambipolar diffusion of photoexcited carriers in bulk GaAs, Appl. Phys. Lett. **97**, 262119 (2010).

[22] D. Paget, F. Cadiz, A. C. H. Rowe, F. Moreau, S. Arscott, and E. Peytavit, Imaging ambipolar diffusion of photocarriers in GaAs thin films, J. Appl. Phys. **111**, 123720 (2012).

[23] R. Okazaki, A. Horikawa, Y. Yasui, and I. Terasaki, Photo-Seebeck effect in ZnO, J. Phys. Soc. Jpn. **81**, 114722 (2012).

[24] P. Price, Ambipolar thermodiffusion of electrons and holes in semiconductors, Lond. Edinb. Dubl. Phil. Mag. J. Sci. **46**, 1252 (1955).

[25] Y. G. Gurevich, O. Y. Titov, G. N. Logvinov, and O. I. Lyubimov, Nature of the thermopower in bipolar semiconductors, Phys. Rev. B **51**, 6999 (1995).

[26] H. J. Goldsmid, *Introduction to Thermoelectricity*, Springer Series in Materials Science (Springer Berlin Heidelberg, Berlin, Heidelberg, 2016), Vol. 121.

[27] G. Wachutka, Rigorous thermodynamic treatment of heat generation and conduction in semiconductor device modeling, IEEE Trans. Comput.-Aided Des. Integr. Circuits Syst. **9**, 1141 (1990).

[28] A. Delamarre, L. Lombez, and J.-F. Guillemoles, Contactless mapping of saturation currents of solar cells by photoluminescence, Appl. Phys. Lett. **100**, 131108 (2012).

[29] P. Wurfel, The chemical potential of radiation, J. Phys. C: Solid State Phys. **15**, 3967 (1982).

[30] H. Esmaielpour, D. Suchet, L. Lombez, A. Delamarre, S. Boyer-Richard, A. Beck, A. Le Corre, O. Durand, and J.-F. Guillemoles, in *2020 47th IEEE Photovoltaic Specialists Conference (PVSC)* (Institute of Electrical and Electronics Engineers (IEEE), Calgary, AB, Canada, 2020), p. 0747, https://ieeexplore.ieee.org/abstract/document/9300544.

[31] H. Esmaielpour, L. Lombez, M. Giteau, J.-F. Guillemoles, and D. Suchet, Impact of excitation energy on hot carrier properties in InGaAs multi-quantum well structure, Prog. Photovolt.: Res. Appl. **30**, 1354 (2022).

[32] Y. P. Varshni, Temperature dependence of the energy gap in semiconductors, Physica **34**, 149 (1967).

[33] A. Le Bris, L. Lombez, S. Laribi, G. Boissier, P. Christol, and J.-F. Guillemoles, Thermalisation rate study of GaSb-based heterostructures by continuous wave photoluminescence and their potential as hot carrier solar cell absorbers, Energy Environ. Sci. **5**, 6225 (2012).

[34] B. A. Ruzicka, S. Wang, L. K. Werake, B. Weintrub, K. P. Loh, and H. Zhao, Hot carrier diffusion in graphene, Phys. Rev. B **82**, 195414 (2010).

[35] P. Yuan, J. Liu, R. Wang, and X. Wang, The hot carrier diffusion coefficient of sub-10 nm virgin MoS_2: Uncovered by non-contact optical probing, Nanoscale **9**, 6808 (2017).

[36] Z. Guo, Y. Wan, M. Yang, J. Snaider, K. Zhu, and L. Huang, Long-range hot-carrier transport in hybrid perovskites visualized by ultrafast microscopy, Science **356**, 59 (2017).

[37] J. Fast, Y.-P. Liu, Y. Chen, L. Samuelson, A. M. Burke, H. Linke, and A. Mikkelsen, Optical-beam-induced current in InAs/InP nanowires for hot-carrier photovoltaics, ACS Appl. Energy Mater. **5**, 7728 (2022).

[38] G. P. Agrawal and N. K. Dutta, *Semiconductor Lasers* (Springer US, Boston, MA, 1993).

[39] C. Smith, R. A. Abram, and M. G. Burt, Theory of Auger recombination in a quantum well heterostructure, Superlattices Microstruct. **1**, 119 (1985).

[40] L. D. Hicks, T. C. Harman, X. Sun, and M. S. Dresselhaus, Experimental study of the effect of quantum-well structures on the thermoelectric figure of merit, Phys. Rev. B **53**, R10493 (1996).

[41] N. Pottier, *Physique Statistique Hors d'équilibre*, Savoirs Actuels (EDP Sciences/CNRS Editions, 2007).

[42] B. Bennett, R. Soref, and J. Del Alamo, Carrier-induced change in refractive index of InP, GaAs and InGaAsP, IEEE J. Quantum Electron. **26**, 113 (1990).

[43] D. S. Chemla, Two-dimensional semiconductors: Recent development, J. Lumin. **30**, 502 (1985).

[44] F. Gibelli, L. Lombez, and J.-F. Guillemoles, Accurate radiation temperature and chemical potential from quantitative photoluminescence analysis of hot carrier populations, J. Phys.: Condens. Matter **29**, 06LT02 (2016).

[45] R. Storn, Differential evolution—a simple and efficient heuristic for global optimization over continuous spaces, J. Glob. Optim. **11**, 341 (1997).

[46] P. Wurfel and U. Wurfel, *Physics of Solar Cells: From Basic Principles to Advanced Concepts* (Wiley-VCH Verlag GmbH & Co. KGaA, Weinheim, 2016), 3rd ed.